Position detection and vibration monitoring system using quad-cell optical beam power distribution

Article *in* Journal of the Franklin Institute · January 2010

DOI: 10.1016/j.jfranklin.2010.04.009

3 authors:

Yasmine El-Ashi
American University of Sharjah
3 PUBLICATIONS **15** CITATIONS
SEE PROFILE

T. Landolsi
American University of Sharjah
66 PUBLICATIONS **769** CITATIONS
SEE PROFILE

Rached Dhaouadi
American University of Sharjah
71 PUBLICATIONS **1,572** CITATIONS
SEE PROFILE

Available online at www.sciencedirect.com
ScienceDirect
Journal of the Franklin Institute 348 (2011) 1435–1455
Journal of The Franklin Institute
www.elsevier.com/locate/jfranklin

Position detection and vibration monitoring system using quad-cell optical beam power distribution

Yasmine El-Ashi*, Taha Landolsi, Rached Dhaouadi

American University of Sharjah, College of Engineering, P.O. Box 26666, Sharjah, UAE

Available online 16 April 2010

Abstract

In this paper, we study the accuracy of an optical vibration sensing system using Gaussian beam analysis. The proposed optical system uses a He–Ne laser source whose Gaussian beam impinges on a quad-cell photodetector array. The normalized optical power for each cell is obtained through numerical simulation based on the well-known Gaussian beam optics formulation, as the beam scans the plane of the photodetectors due to vibration. The system detection principle lies upon finding a relationship between the power distribution of the quad-cell and the position of the beam centroid, which allows us to identify the characteristics of the vibration applied, such as direction, frequency and strength. The aspects of practical implementation and experimental limitations on the power distribution accuracy are discussed and the discrepancies with the theoretical results are presented.

Keywords: Vibration montioring; Gaussian laser beam; Position detection; Optical power; Quad-cell

1. Introduction

In the recent years, vibrometry has become crucially important in a wide range of applications such as the detection of buried land mines and roadside bombs, monitoring the mechanical aging or health conditions of equipment and machinery [1], as well as exploratory testing to determine certain characteristics of a product [2]. In addition, vibration monitoring is a versatile field in industry where the vibrations induced by industrial equipment, heavy rotating machinery in power stations, as well as the process of drilling oil and gas wells need to be continuously detected and measured to avoid any

*Corresponding author. Tel.: +971 509655766.
E-mail address: g00007313@aus.edu (Y. El-Ashi).

0016-0032/$32.00
doi:10.1016/j.jfranklin.2010.04.009

hazardous results. Furthermore, rotor vibrations and electric motors can have a damaging effect on the quality of manufactured articles in the production process, which makes it vitally necessary for engineers to consider performance evaluation, control and suppression of machine vibration [4]. Lately, optical and laser vibrometry has received great attention as a beneficial tool that would enhance the achievement of the preceding goals in a non-contact and remote setup.

Substantial research has been conducted on several vibration sensors such as standard strain gauges, piezoelectric accelerometer, homodyne laser vibrometers and optical fiber sensors. The piezoelectric accelerometer is one of the most common vibration sensors used for monitoring the dynamic characteristics of structures in the presence of external disturbance. It is basically an electromechanical device that generates an output voltage proportional to an applied vibratory acceleration [3]. These type of sensors can be advantageous in terms of accuracy and sensitivity, however they cover a relatively small area and can be cumbersome as well as unsuitable in certain applications surrounded by electrical and magnetic fields, due to the difficulty encountered in electrically isolating them. Optical vibration sensors offer an alternative option for such purposes, owing to their superiority of electromagnetic interference immunity, corrosion resistance, safe operation in explosive, high temperature, and hazardous environment, chemically inert and light weight. Nevertheless, any methodology has its limitations, where in the case of optical vibrometry, the drawbacks include direct sensitivity to variations in the intensity of the light source and dependence on ambient conditions, such as ambient light, smoke, dirt and moisture [2].

In this paper we propose an optical vibrometer based on the detection of the position of the center of a Gaussian laser beam projected on a quad-cell photodetector array. Since only the optical power of each photocell can be practically acquired, we aim to find a relationship between the power distribution of the photodetector array and the position of the beam center. The main contribution of our work involves extensive mathematical analysis and simulation to model the proposed system theoretically, in order to obtain closed form equations which relate optical power detected by the photocells to the x and y positions of the center of the beam. In addition an experimental setup was implemented to validate the theoretical model.

To achieve a more accurate system model and to depict a better comparison between the theoretical results and experimental measurements, our approach takes into consideration the circular shape of the beam spot projected onto the array of photocells and the Gaussian intensity profile of the spot in formulating the optical power equations. Furthermore, system imperfections such as the gap separations between the photocells have been accounted for in the simulation and their effect on the optical power distribution is studied. The proposed methodology for position detection of the beam center will enable us to identify the direction of the vibration applied to the system, and to quantify its level as well as frequency characteristics.

The rest of the paper will be structured as follows: in Section 2, we give an overview of the proposed optical vibration sensor hardware architecture. In Section 3, the mathematical formulation and simulation of the system model for evaluating the normalized power distribution of the quad-cell array will be presented. Moreover, we will discuss the impact of the practical limitations on the simulated power distribution. The accuracy reduction in the position of the beam centroid and the discrepancies observed in the optical power between the case where interspatial quad-cell gaps are

introduced in the experimental configuration and that of the ideal system model will be investigated. Finally, Section 4, involves a discussion of the experimental setup and results.

2. System hardware model

The system we are considering, as shown in Fig. 1, mainly consists of a laser beam source with a wavelength $\lambda = 633\,\text{nm}$, mounted on two actuators, for azimuthal and vertical motion steering. The Gaussian beam emitted from the source is incident on to a fixed photodetector array, which captures the light intensity distribution, and generates certain current outputs. Next, the optical power information of each photodetector cell is input to an optical system acquisition and vibration monitoring system, which yields an estimate of the centroid coordinates of the laser beam, and accordingly detects the direction of vibration. A two-dimensional beam steering mechanism, will also be deployed to automatically steer the laser beam to the initial location when appropriate.

The design problem at hand involves two crucial parts. The first part is mainly concerned with sensing the position of the laser beam centroid, while the second part utilizes the position data to monitor the direction of vibration. The latter approach to the problem involves finding an inverse relationship between the optical power distribution and the position of the laser beam centroid. To achieve such a goal, the forward problem of the preceding system must be evaluated first, that is calculate the optical power as the centroid of the beam is scanned throughout the plane of photocells. Since, optical power is directly proportional to the incident area of overlap between the photodetector and the beam ($P = \int I\,dA$), closed form equations for the area of intersection for one photodetector cell have been obtained for analytical purposes.

The next step is to compute the optical power covered by the required area of overlap between the detector active surface and the beam disk, given that the intensity of the beam is characterized by a Gaussian profile. Finally, having evaluated the optical power as the beam is scanned across one photodetector cell, the system model will be extended further

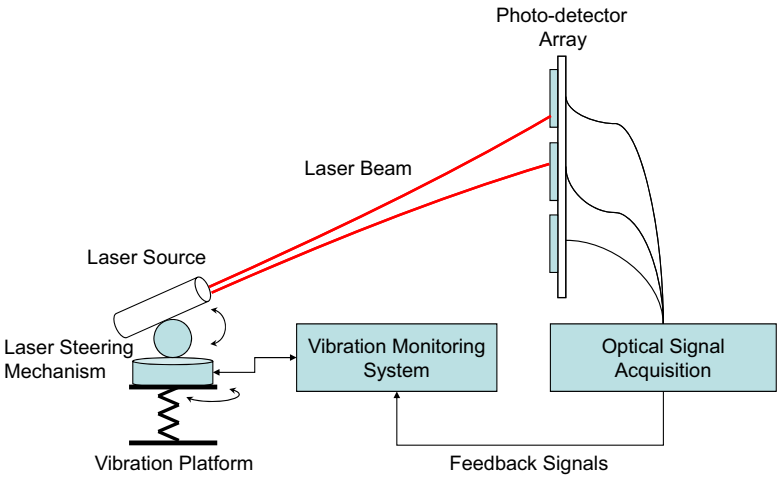

Fig. 1. Hardware architecture of the proposed optical vibrometer.

to account for an array of four photodiodes, where the optical power for each one will be calculated as the centroid of the beam disk moves along the plane covered by the quad-cell.

The following discussion involves a detailed derivation of the closed form equations for optical power, as the centroid of the beam moves along the x-axis only, y-axis only, and both x- and y -axes, on the plane covered by one photocell. Based on that, the optical power distribution for four photocells is evaluated, and the effect of introducing vertical and horizontal spacing between them will be examined.

3. Simulation

The laser beam incident on to a 1 cm × 1 cm square photodetector cell is modeled as a circular disk with a radius, $\rho_0 = 0.5$ cm. A code has been developed using Matlab, to compute the interception area between the beam disk and the photodetector as the beam centroid is moved anywhere outside and inside the boundaries of the square cell. The position of the centroid is determined with respect to an absolute $x-y$ coordinate system, where its origin is located at the center of the photodetector.

To calculate the area through simulation, certain supporting parameters such as the number of points of intersection between the circular disk and the square cell N_{int}, as well as the number of corners of the square that lie within the circle N_c, were found.

Next, we will discuss the mathematical formulation necessary for obtaining the closed form equations for the overlap area. This will be divided into three categories: (1) finding the area of intersection while moving the disk along the x direction only, (2) finding the area of intersection while the disk is moved along the y direction only, and finally (3) finding the area of intersection as the disk is moved along the entire $x-y$ plane, along any random path. By referring to Fig. 2, given that $\alpha_2 = \pi-\alpha_1$, $\rho_1(\alpha) = (x-x_0)/\sin\alpha$, and $\rho_2(\alpha) = \rho_0$, we can calculate the intersection area A_x using

$$A_x = \int_{\alpha_1}^{\alpha_2} \int_{\rho_1(\alpha)}^{\rho_2(\alpha)} \rho \, d\rho \, d\alpha = \frac{\rho_0^2}{2}[\pi-2\alpha_1-\sin 2\alpha_1] \tag{1}$$

Using $\beta_2 = \pi-\beta_1$, $\rho_1(\beta) = (y-y_0)/\sin\beta$, and $\rho_2(\beta) = \rho_0$, the intersection area A_y indicated by the shaded region in Fig. 3, as the disk moves along the vertical y-axis only, can be

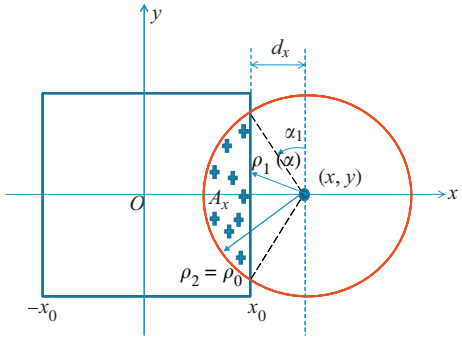

Fig. 2. Parameters definition for area A_x.

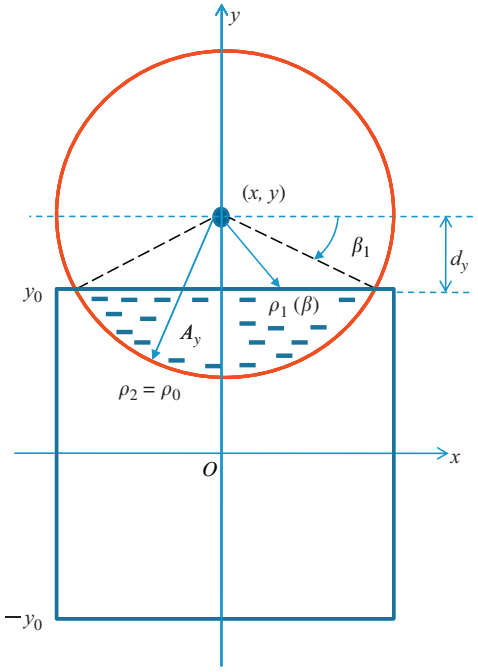

Fig. 3. Parameters definition for area A_y.

stated as follows:

$$A_y = \int_{\beta_1}^{\beta_2} \int_{\rho_1(\beta)}^{\rho_2(\beta)} \rho \, d\rho \, d\beta = \frac{\rho_0^2}{2}[\pi - 2\beta_1 - \sin 2\beta_1] \tag{2}$$

To derive the area of intersection A_{xy} as the disk is moved along both the x- and y -axes of the photodetector plane, the parameters α_1, β_1, $d_x = x - x_0$, $d_y = y - y_0$, $\phi = \tan^{-1}(d_y/d_x)$, $\rho_x = (x - x_0)/\sin\alpha$, and $\rho_y = (y - y_0)/\sin\beta$ are first evaluated to yield the following result:

$$A_{xy} = A_1 + A_2 = \int_{\phi+\pi/2}^{\alpha_2} \int_{\rho_x}^{\rho_0} \rho \, d\rho \, d\alpha + \int_{\pi-\phi}^{\beta_2} \int_{\rho_y}^{\rho_0} \rho \, d\rho \, d\beta$$

$$= \frac{\rho_0^2}{2}\left[\frac{\pi}{2} - (\alpha_1 + \beta_1) - \frac{\sin\alpha_1}{\cos\phi}\cos(\alpha_1 + \phi) - \frac{\sin\beta_1}{\sin\phi}\sin(\phi - \beta_1)\right] \tag{3}$$

where as shown in Fig. 4 (x,y) indicate the coordinates of the center of the circular disk with respect to the center of the square photodetector cell, and (x_0,y_0) represent the coordinates of the top right-most corner of the photocell, which in this case $x_0 = 0.5$ and $y_0 = 0.5$.

3.1. Gaussian beam model

The optical signal emanating from the laser source is commonly modeled as a Gaussian beam whose intensity varies with the propagation distance z and the radius of the beam, measured from its center, as follows [5,7]:

$$I(\rho,z) = I_0\left[\frac{W_0}{W(z)}\right]^2 \exp\left[-\frac{2\rho^2}{W^2(z)}\right] \tag{4}$$

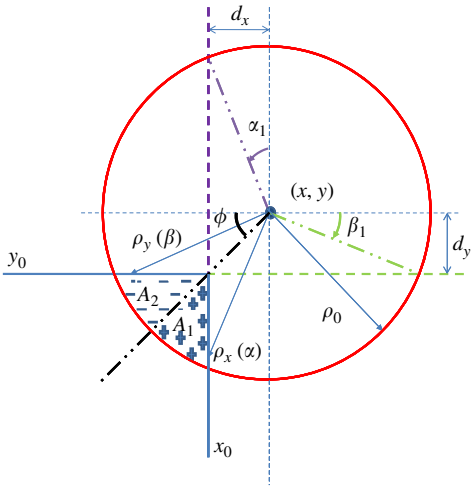

Fig. 4. Parameters definition for area A_{xy}.

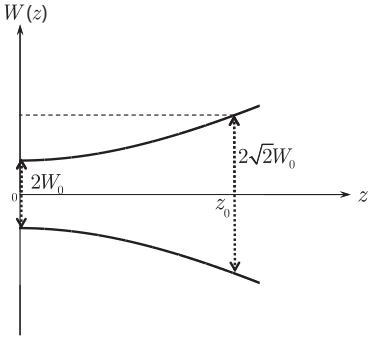

Fig. 5. Gaussian beam model for the laser source used in the proposed vibrometer.

Here, I_0 is the maximum beam intensity measured in the center of the beam, $\rho = \sqrt{x^2 + y^2}$ is the minimum waist of the beam assumed to occur at distance ρ and $W(z)$ is the beam waist at distance z. If the Rayleigh range of the beam is noted z_0 and the optical wavelength λ, then the beam waists are given by $W_0 = \sqrt{\lambda z_0/\pi}$ and $W(z) = W_0\sqrt{1 + (z/z_0)^2}$. These beam characteristics are illustrated in Fig. 5 which clearly shows the diffraction of Gaussian beams in free-space. As the laser beam propagates, its power remains constant but its intensity decreases with an inverse-square law. This behavior is important to consider in the design of the experimental setup because the power intercepted by the photodetector depends on the area of the detector active surface and on the beam waist at the distance separating the beam minimum waist location, i.e. $z = 0$, and the location z of the photodetector. A circle of radius ρ_0 on the photodetector will intercept a portion of the

total beam power P_T given by

$$\frac{1}{P_T}\int_0^{2\pi}\int_0^{\rho_0} I(\rho,z)\rho\, d\rho\, d\alpha = 1-\exp\left[-\frac{2\rho_0^2}{W^2(z)}\right] \tag{5}$$

The power contained within a circle of radius $\rho_0 = W(z)$ is approximately 86% of the total power. About 99% of the power is contained within a circle of radius $1.5W(z)$. Since the radius of the circular disk is $\rho_0 = 0.5$ cm, then to achieve 99% of the total power W_0 was set to 1/3 cm.

3.2. Optical power analytical estimation

The optical power enclosed within a certain area of intersection is derived for three different cases, the power as the beam moves along the x direction only, the y direction only, and both $x-y$ directions. Using

$$P_x = \int_{\alpha_1}^{\alpha_2}\int_{\rho_1(\alpha)}^{\rho_2(\alpha)} I_0\left[\frac{W_0}{W(z)}\right]^2 \exp\left(\frac{-2\rho^2}{W^2(z)}\right)\rho\, d\rho\, d\alpha \tag{6}$$

And, given that $I_1 = I_0[W_0/W(z)]^2$, $\rho_2(\alpha) = \rho_0$ and $\rho_1(\alpha) = (x-x_0)/\sin\alpha$ then the power for horizontal motion can be stated as

$$P_x = -\kappa_1\kappa_2(\alpha_2-\alpha_1) + \kappa_1\int_{\alpha_1}^{\alpha_2}\exp\left(-\frac{\kappa_x}{\sin^2\alpha}\right)d\alpha \tag{7}$$

where

$$\kappa_x = \frac{2}{W^2}(x-x_0)^2$$

$$\kappa_1 = I_1\left(\frac{W}{2}\right)^2$$

$$\kappa_2 = \exp\left(-\frac{2\rho_0^2}{W^2}\right)$$

The power while the beam is moved along the y direction only can be determined using the following:

$$P_y = \int_{\beta_1}^{\beta_2}\int_{\rho_1(\beta)}^{\rho_2(\beta)} I_0\left[\frac{W_0}{W(z)}\right]^2 \exp\left(\frac{-2\rho^2}{W^2(z)}\right)\rho\, d\rho\, d\beta \tag{8}$$

Provided that, $\rho_2(\beta) = \rho_0$ and $\rho_1(\beta) = (y-y_0)/\sin\beta$, the optical power can be written as

$$P_y = -\kappa_1\kappa_2(\beta_2-\beta_1) + \kappa_1\int_{\beta_1}^{\beta_2}\exp\left(-\frac{\kappa_y}{\sin^2\beta}\right)d\beta \tag{9}$$

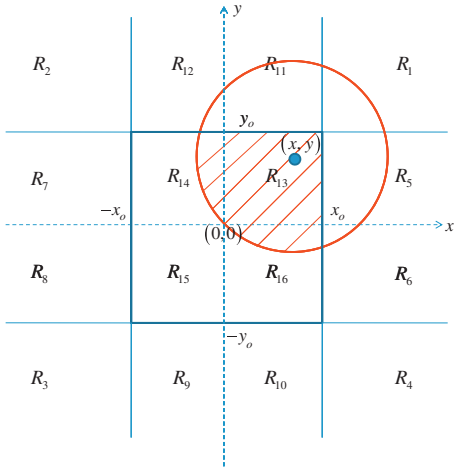

Fig. 6. Example of beam centroid position as it scans the photocells region.

where $\kappa_y = (2/W^2)(y-y_0)^2$. Finally, as the beam is moved along both the x and y directions along the entire plane of one photocell, the power can be calculated as

$$P_{xy} = P_1 + P_2 = \int_{\phi+\pi/2}^{\alpha_2}\int_{\rho_x}^{\rho_0} I(\rho,z)\rho\, d\rho\, d\alpha + \int_{\pi-\phi}^{\beta_2}\int_{\rho_y}^{\rho_0} I(\rho,z)\rho\, d\rho\, d\beta$$
$$= -\kappa_1\kappa_2\left[\frac{\pi}{2} - (\alpha_1+\beta_1)\right] + \kappa_1\int_{\phi+(\pi/2)}^{\alpha_2} \exp\left(-\frac{\kappa_x}{\sin^2\alpha}\right)d\alpha$$
$$+ \kappa_1\int_{\pi-\phi}^{\beta_2} \exp\left(-\frac{\kappa_y}{\sin^2\beta}\right)d\beta \tag{10}$$

The integrals in the preceding equations were evaluated numerically.

Using Eqs. (7), (9), and (10) an algorithm has been developed to determine the power P if the centroid of the circular disk is to be moved along any random path. To do this, the plane for one photocell has been divided into 16 different regions as shown in Fig. 6. The power is computed depending on the region where the centroid of the beam is located.

if $(x, y) \in R_1, R_2, R_3$, or R_4 **then**
  The power of the shaded region is $P = P_{xy}$
else if $(x, y) \in R_5, R_6, R_7$, or R_8 **then**
  Check the following:
  if $N_c = 1$ and $N_{int} = 2$ **then**
  Check the following:
  if $d_x \neq 0$ and $d_y \neq 0$ or $d_x \neq 0$ and $d_y = 0$ or $d_x = 0$ and $d_y \neq 0$ **then**
    $P = P_x - P_{xy}$
  else if $d_x = 0$ and $d_y = 0$ **then**
    The power of the shaded region is $P = \frac{1}{4}P_T$.
  else if $N_c = 0$ and $N_{int} = 2$ **then**
    The power of the shaded region is $P = P_x$.
  end if

else if $(x, y) \in R_9, R_{10}, R_{11}$, or R_{12} **then**
  Check the following:
  if $N_c = 1$ and $N_{int} = 2$ **then**
    Check the following:
    if $d_x \neq 0$ and $d_y \neq 0$ or $d_x \neq 0$ and $d_y = 0$ or $d_x = 0$ and $d_y \neq 0$ **then**
      The power of the shaded region is $P = P_y - P_{xy}$.
    else if $d_x = 0$ and $d_y = 0$ **then**
      The power of the shaded region is $P = \frac{1}{4} P_T$.
    end if
else if $N_c = 0$ and $N_{int} = 2$ **then**
    The power of the shaded region is $P = P_y$.
  end if
else if $(x, y) \in R_{13}, R_{14}, R_{15}$, or R_{16} **then**
  Check the following:
  if $N_c = 1$ and $N_{int} = 2$ **then**
    The power of the shaded region is $P = P_T - (P_x + P_y - P_{xy})$.
  else if $N_c = 0$ and $N_{int} = 4$ **then**
    The power of the shaded region is $P = P_T - (P_x + P_y)$.
  end if
end if

where $P_T = 2\pi I_1 [W/2]^2 (1-\kappa_2)$ is the total power of the disk with radius 0.5 cm [6].

3.3. *Effect of quad-cell gaps on power distribution*

The quad-cell array of photodetectors has been modeled as the orientation shown in Fig. 7. Each photocell is represented as a 1 cm × 1 cm square, with centers S_1, S_2, S_3 and S_4. The photocells are separated by a small horizontal distance ε and a vertical distance δ. In this case, the origin of the absolute Cartesian coordinate system is located at the center of the array. The coordinates of S_1, S_2, S_3 and S_4 with respect to the

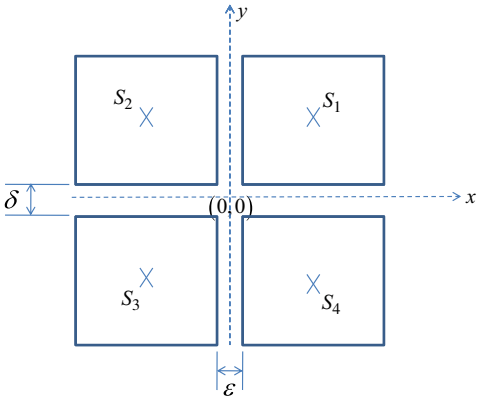

Fig. 7. Quad-cell array of photodetectors.

origin are

$$S_1 = \begin{bmatrix} x_1 \\ y_1 \end{bmatrix} = \begin{bmatrix} 0.5 + \varepsilon/2 \\ 0.5 + \delta/2 \end{bmatrix}$$

$$S_2 = \begin{bmatrix} x_2 \\ y_2 \end{bmatrix} = \begin{bmatrix} -0.5-\varepsilon/2 \\ 0.5 + \delta/2 \end{bmatrix}$$

$$S_3 = \begin{bmatrix} x_3 \\ y_3 \end{bmatrix} = \begin{bmatrix} -0.5-\varepsilon/2 \\ -0.5-\delta/2 \end{bmatrix}$$

$$S_4 = \begin{bmatrix} x_4 \\ y_4 \end{bmatrix} = \begin{bmatrix} 0.5 + \varepsilon/2 \\ -0.5-\delta/2 \end{bmatrix}$$

The main objective of the problem at hand is to obtain the optical power distribution generated at each photodetector while the beam is scanned throughout the entire quad-cell plane, thus an algorithm has been deployed to calculate the optical power for each cell. The mathematical model mentioned in the previous discussion has been obtained while considering the origin of the $x-y$ coordinate system situated at the center of one photocell. Therefore, to evaluate the optical power for the quad-cell using Eqs. (7), (9), and (10), the origin of the absolute coordinate system will be translated by a certain vector determined by the coordinates of the center of the cell. The portion of power captured by each cell is calculated. To find the power distribution for cell 1 in the array, the translational operation (x,y)–(x_1,y_1) is first made. Then the earlier power calculations are carried out on photocell 1. A similar translation is applied to the second, third and fourth cell, where the power distribution is evaluated for each cell separately (Fig. 7).

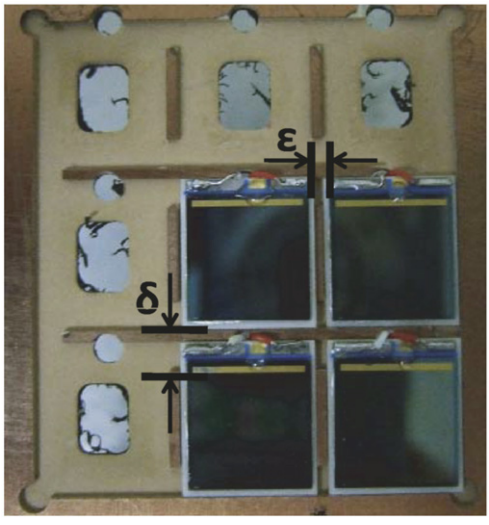

Fig. 8. Quad-cell arrangement for experimental setup where ε and δ are not equivalent.

Furthermore, the centroid of the beam disk has been simulated to move on the plane of photodetectors with a speed of 1 cm/s, along the trajectory $y=x$, within a time interval of 4 s. A plot of the optical power distribution for the four cells against time, following the given trajectory can be shown in Fig. 9, where ε and δ are first set to zero. As illustrated, the beam occupies most of the active surface areas of photocells 1 and 3, and as it moves away from photocell 3 and into the vicinity of photocell 1, cells 2 and 4 start detecting a portion of the optical power. All four cells will ideally detect equal powers when the centroid of the beam is at the origin of the plane. Since the values for ε and δ are technically not equal to zero, their effect on the overall power distribution was investigated.

Another simulation has been run, when $\varepsilon = \delta = 0.1$ and 0.2 cm. As shown in Fig. 9, the maximas of the normalized power waveforms for the first and third photocells shifted to their new center positions, at (0.55,0.55) and (−0.55,−0.55) for $\varepsilon = \delta = 0.1$ cm, and at (0.6,0.6) and (−0.6,−0.6) for $\varepsilon = \delta = 0.2$ cm. In addition, the power at the origin drops exponentially as ε and δ become larger. This effect has been demonstrated in Fig. 10. The value for ε was varied from 0 to 0.9 cm in steps of 0.1 cm. The normalized power at one of the photocells has a maximum value of 0.25 at $\varepsilon = \delta = 0$ cm. With a spacing of 0.1 cm, the power at the origin of the plane dropped by 41.96% from its maximum value, and for $\varepsilon = \delta = 0.2$ cm, we have a 70.44% power drop. Another observation that can be made is that, as the gap between the photocells increase the time delay between photocells 1 and 3 attaining maximum power will also increase. If the beam is moving with a speed of v cm/s,

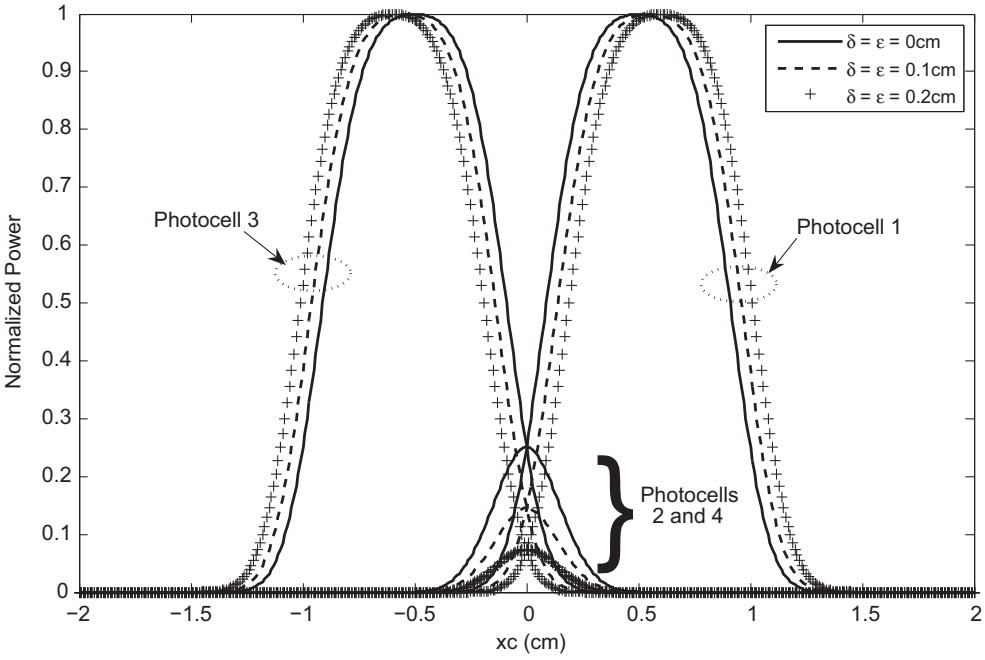

Fig. 9. Variation of the optical power detected by all four photodetectors as the beam is moved along $y=x$ line for different values of ε and δ.

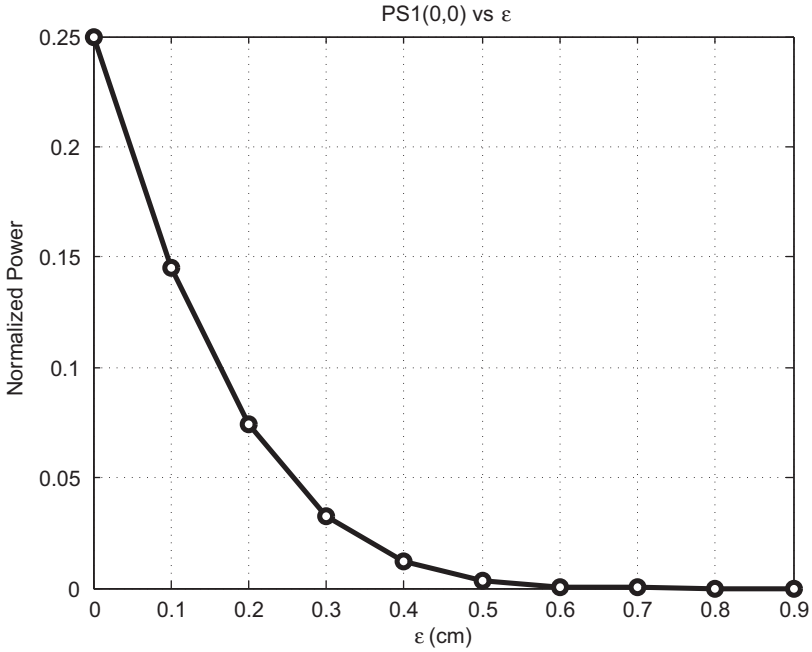

Fig. 10. Plot of normalized power for photocell 1 vs. ε, when the beam centroid is at the origin of the quad-cell plane. ε and δ are assumed to be equal.

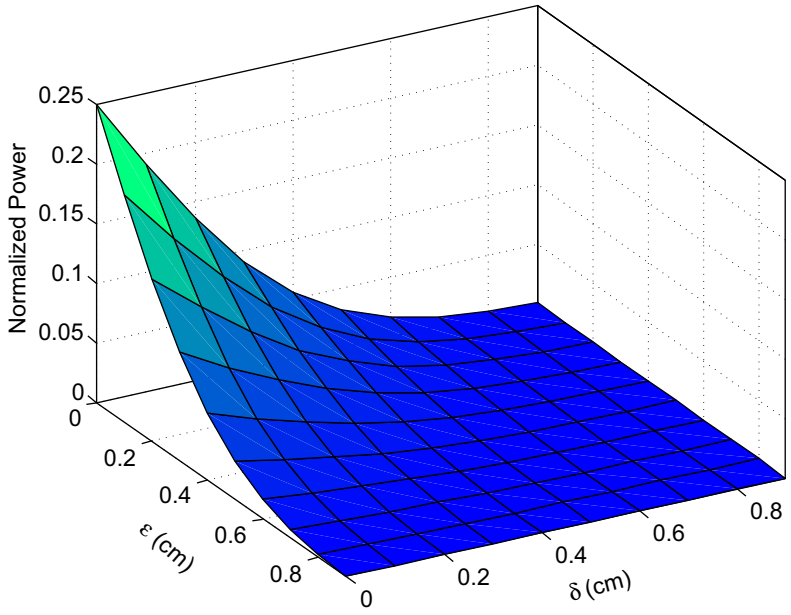

Fig. 11. Plot of normalized power for photocell 1 vs. ε and δ, when the beam centroid is at the origin of the quad-cell plane.

the time delay can be described by the following equation:

$$\tau(v,\varepsilon,\delta) = \frac{1}{v}\sqrt{(1+\varepsilon)^2 + (1+\delta)^2} \tag{11}$$

In the previous discussion, ε and δ were equal, however the design of the experimental setup inevitably defies such an assumption. As shown in Fig. 8, the photocells are placed on a metallic plate with substrates of size 1.1 cm × 1.3 cm. The spacing between them is 1 mm. Thorlabs FDS1010 photodiodes have been used, where the Si detector is mounted on a 1.1 cm × 1.3 cm ceramic wafer with an anode and a cathode. The active area for the FDS1010 is about 9.7 mm × 9.7 mm [8]. Taking into account the width of the inactive region of the photocell, would add an extra 0.2 cm to the vertical spacing between the photodiodes. Therefore, the experimental values for ε and δ can be approximated to 0.1 and 0.3 cm. Using those values in the simulation, gave us a normalized power of 0.069 at the origin of the quad-cell plane. This is about 72.4% power drop when compared to the ideal case, and 52.45% power drop relative to the case when $\varepsilon = \delta = 0.1$ cm (Fig. 11).

4. Experimental results

4.1. Description of the experimental setup

In order to verify the theoretical results for the normalized power distribution for the quad-cell array obtained through simulation, a laboratory prototype of the optical power detection system has been designed (Fig. 12).

The experimental setup in Fig. 12 can be divided into three main parts; the optical setup and XY stage as shown in Figs. 13, 14 and 15 and the data acquisition system shown in Fig. 16. The transmitter optics consists of a single mode fiber cable, where one of its ends is connected to a He–Ne laser source, and the other end is coupled to a collimator. The fiber cable acts as a spatial filter at a wavelength of 633 nm, which removes higher modes so that only the fundamental mode is left. A collimator (F260FC-B, Thorlabs) is used with a

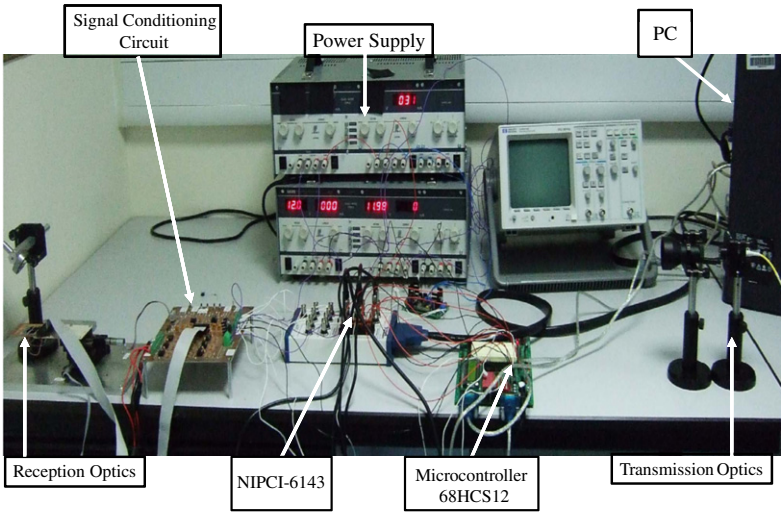

Fig. 12. Experimental prototype of the optical power detection system.

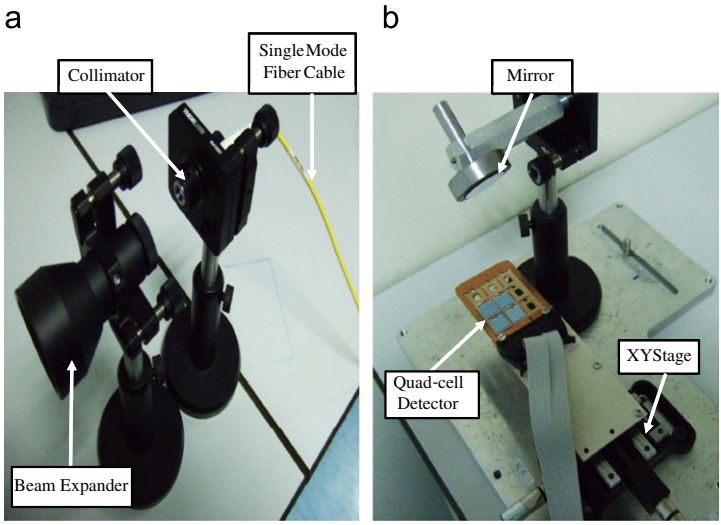

Fig. 13. (a) Transmission optics. (b) Reception optics.

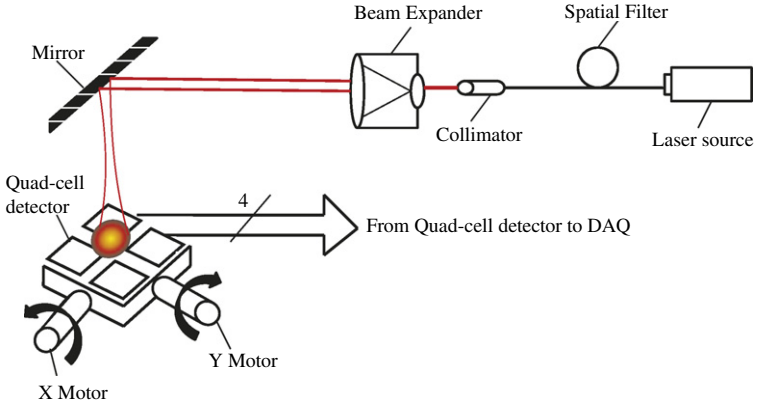

Fig. 14. Optical setup of the system.

633 nm alignment wavelength, where the lens is manufactured to be one focal length away from the output end of the fiber. The laser beam is then projected into a Galilean Beam Expander (BE03M, Thorlabs) which is used to adjust the beam diameter to be the same size as one side of a photocell. On the other hand, the receiver optics is composed of a mirror which reflects the beam on to the quad-cell detector. Each photodiode (FDS1010, Thorlabs) is connected to an RC noise filter with a cut-off frequency of about 10 kHz, and an amplification circuitry as shown in Fig. 15 [8]. The output voltages of the photodiodes are fed into four simultaneously sampled analog input channels of a BNC shielded connecter block (NI BNC-2110, National Instruments) for the Data Acquisition Card (NI PCI-6143, National Instruments), which also provides a 16-bit resolution and a sampling rate of up to 250 kS/s per channel. In addition, to be able to measure the power distribution of the quad-cell detector for different x and y positions for the center of the

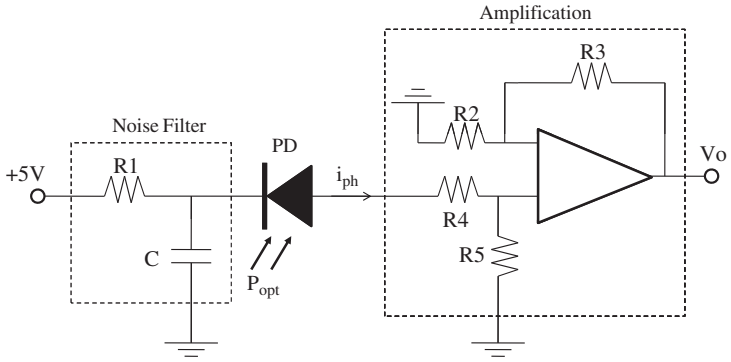

Fig. 15. Signal conditioning circuitry for photodiode, involving amplification and noise removal.

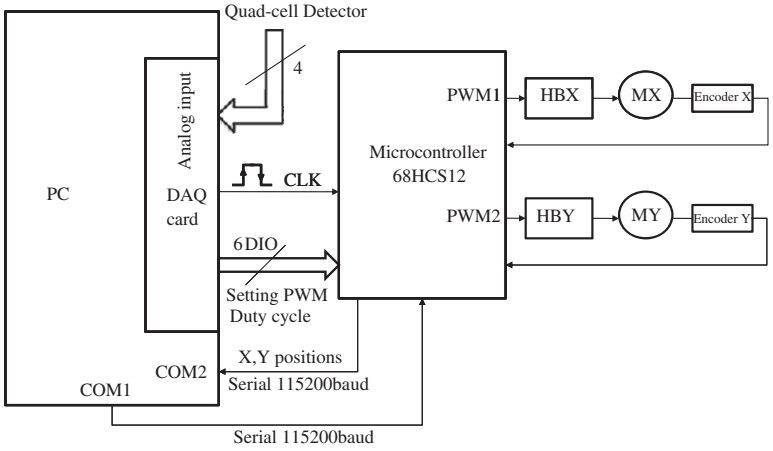

Fig. 16. Block diagram for photo-voltageacquisition and position measurement system (HBX: H-bridge for motor X; HBY: H-bridge for motor Y; MX: motor X; MY: motor Y; PWM1: pulse width modulated signal fed into motor X; PWM2: pulse width modulated signal fed into motor Y; COM1: communication port 1; COM2: communication port 2; CLK: clock to synchronize photo-voltage acquisition and position measurement; DIO: digital input/output channels; PC: personal computer).

beam, the quad-cell array has been mounted on to an XY motorized linear translation stage (T25XY, Thorlabs). The T25XY stage provides a travel range of about 2.5 cm, and utilizes two 12 V DC servomotors with a 256:1 gear reduction head [8]. Furthermore, two PWM signals with a frequency of 330 Hz, and 50% duty cycle, generated by a Dragon 12 (68HCS12) microcontroller via a Dual H-bridge, are used to drive the X and Y motors. The motor mounted 48 pts/rev rotary encoder signals are fed back to the microcontroller to obtain the position measurements. The x and y positions are sent to the PC through a serial port where the baud rate is set to 115.2 kbits/s. The power and position measurements are acquired synchronously every 1 s, for one complete travel range of the Y motor while keeping the X motor fixed at a certain distance.

4.2. Measurement results

To avoid the effect of ambient light on the photocells' output voltage, the experiment has been conducted in darkness. A more effective solution for eliminating the ambient light noise would be provided by the use of a lock-in amplifier. Using the data illustrated in Fig. 17 the calculated RMS (root mean square) value for the output voltage of a photocell in darkness is about; 4.6299e−004 V. Five different runs were carried out by scanning the beam spot along the y-axis of the quad-cell plane, while fixing the x position of the beam center at −1.05, −0.55, 0, 0.55 and 1.05 cm. By referring to Fig. 7 and given that $\varepsilon = 0.1$ cm, the beam spot was first scanned vertically along the left sides of photocells 2 and 3, where the x position of the beam center is −1.05 cm. The second scan was made along the vertical axis passing through the centers S_2 and S_3 of photocells 2 and 3, where $x = -0.55$ cm. Furthermore, a vertical scan at $x = 0$ cm along the y-axis of the array plane was carried out. The last two runs were made along the vertical line $x =$ 0.55 cm passing through the centers S_1 and S_4, and along $x =$ 1.05 cm passing through the right sides of photocells 1 and 4. The output photo-voltage is directly proportional to the optical power sensed by a photocell. The output voltage is derived as

$$V_o = A_v P_{\text{opt}} \mathcal{R}(R_4 + R_5) \tag{12}$$

where A_v is the amplification gain, P_{opt} is the incident optical power and R_4+R_5 is the load resistance. While $\mathcal{R}$ provides an estimate of the amount of photocurrent i_{ph} expected at a certain wavelength λ:

$$i_{\text{ph}} = P_{\text{opt}} \mathcal{R} \tag{13}$$

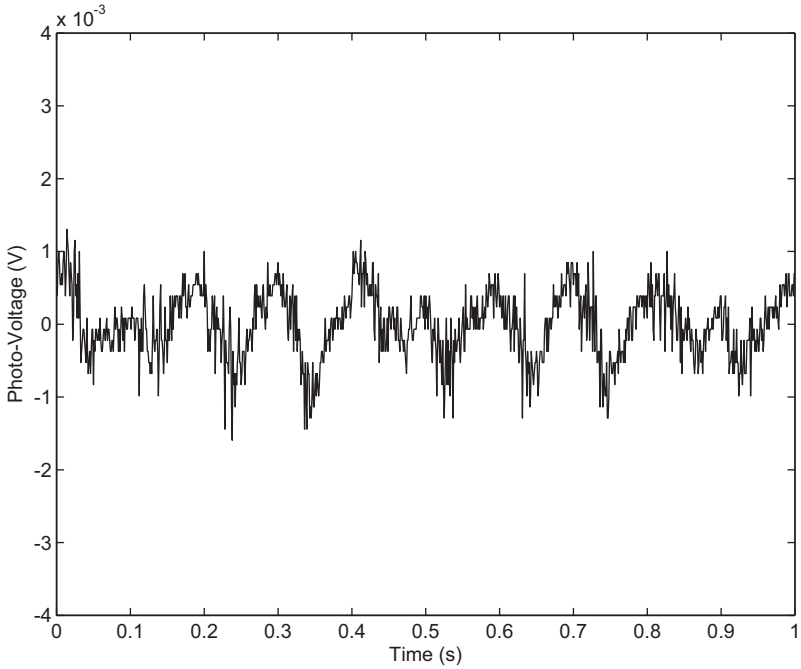

Fig. 17. Plot of photocell output voltage in darkness.

According to typical responsivity curves for photodiode FDS1010, we have $\mathcal{R} \approx 0.35\,\mathrm{A/W}$ for a wavelength of 633 nm [8]. Therefore, given a linear relation between the photocells' optical power and acquired output voltage, the experimental normalized voltage measurements were compared to the theoretical model obtained through simulation by setting ε and δ to 0.1 and 0.3 cm.

At $x = 1.05$ cm, theoretically only photocell 1 will be detecting power as the y position of the beam center $y \geq 0.35$ cm and maximum power which is half of the total normalized power is detected at $y = 0.65$ cm. Photocell 4 starts to pick up power for $y < 0.35$ cm and captures half of the power at $y = -0.65$ cm. According to Fig. 18, the maximum normalized voltage for photocell 1 was reached at $y = 0.71$ cm with a voltage percentage error of 3.7% from the theoretical maximum value. On the other hand, photocell 4 acquired maximum voltage at $y = -0.77$ cm with a voltage percentage error of 3.9%.

In the case where x is fixed to -1.05 cm, only photocell 2 will be detecting power for $y \geq 0.35$ cm, while the power reaches its peak value at $y = 0.65$ cm. In addition, according to the theoretical results photocell 3 detects optical power for $y < 0.35$ cm and acquires half of the power at $y = -0.65$ cm. Practically, by referring to Fig. 19, the peak normalized voltage for photocell 2 was detected at $y = 0.67$ cm with a voltage percentage deviation of 8.9%. The peak normalized voltage for photocell 3 was reached at $y = -0.74$ cm and a percentage error of about 5.9% from the theoretical normalized voltage results (Fig. 20).

At $x = 0.55$ cm, the maximum optical power detected for photocell 1 is at $y = 0.65$ cm, however when compared to the experimental results, the peak value is detected at $y = 0.66$ cm, which gives an approximate percentage error of 2.0% in the y position of the

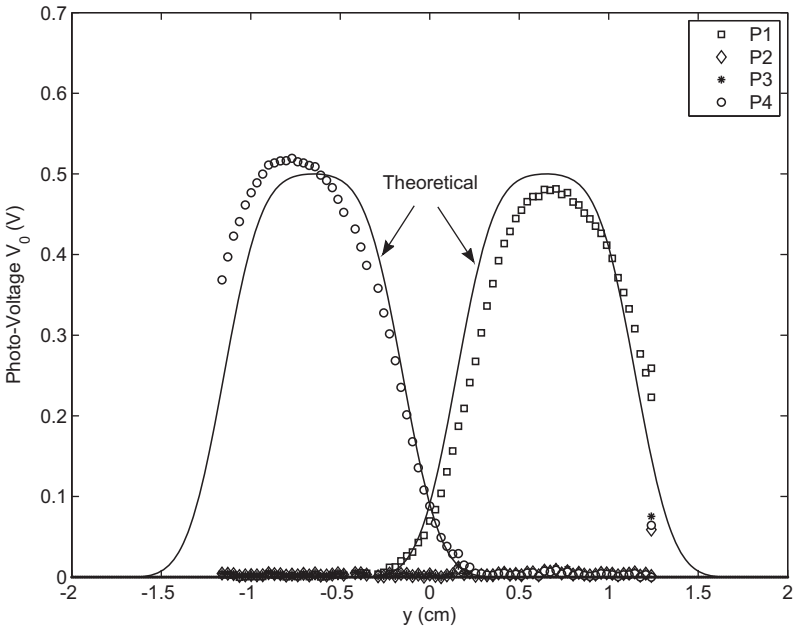

Fig. 18. Plot of photocell output voltage vs. y position of the center of the beam while setting the x position at 1.05 cm.

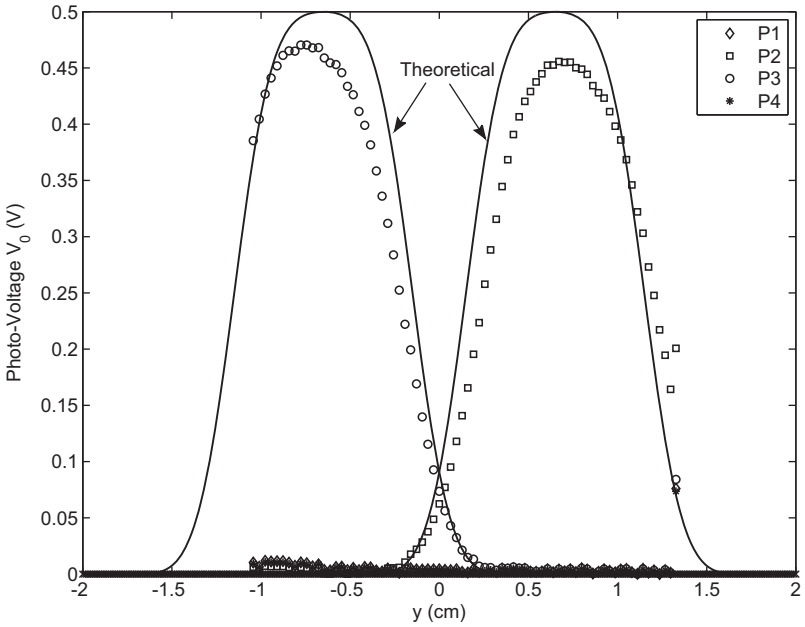

Fig. 19. Plot of photocell output voltage vs. y position of the center of the beam while setting the x position at -1.05 cm.

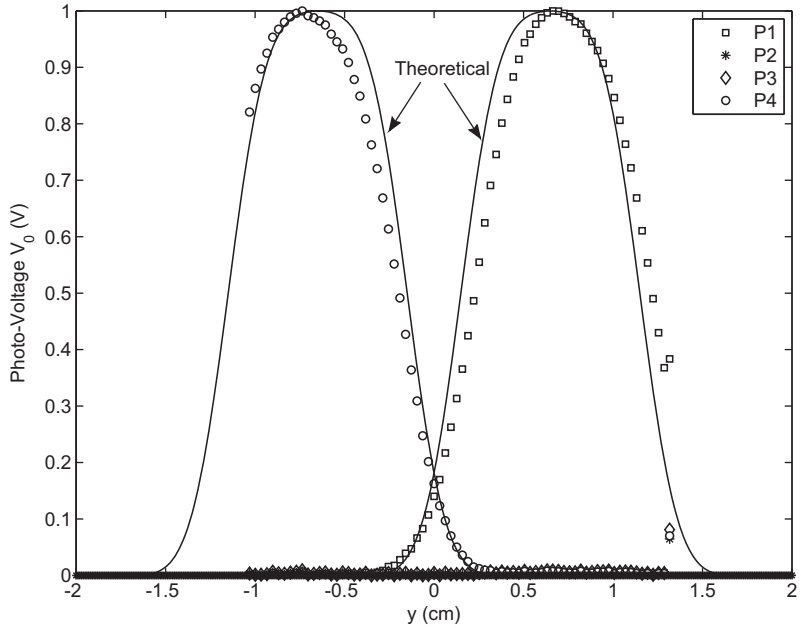

Fig. 20. Plot of photocell output voltage vs. y position of the center of the beam while setting the x position at 0.55 cm.

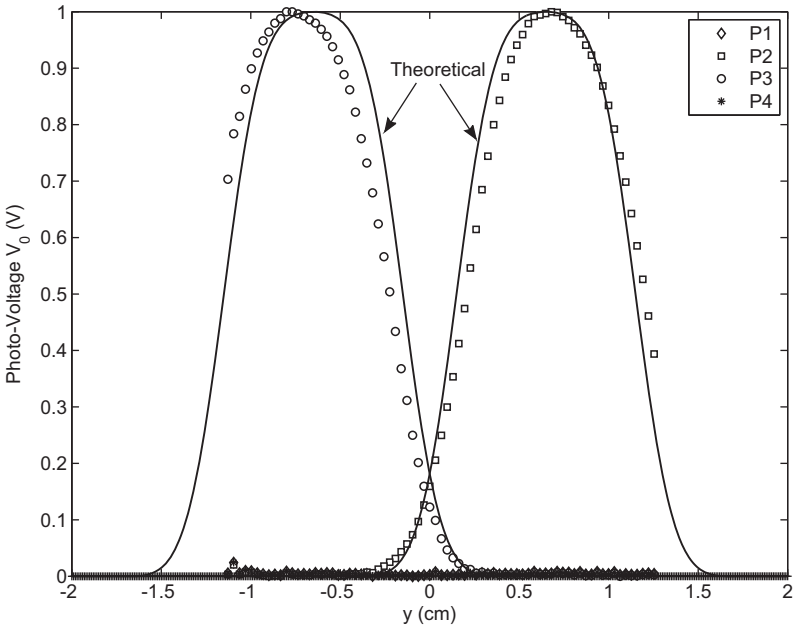

Fig. 21. Plot of photocell output voltage vs. y position of the center of the beam while setting the x position at -0.55 cm.

beam center. For photocell 4 maximum optical power is attained theoretically at $y=-0.65$ cm, while the measured y position for the beam center was $y=-0.74$ cm, hence a percentage error of about 13.3%. In Fig. 21, at $x=-0.55$ cm, the maximum power obtained through experiment for photocell 2 was at $y=0.68$ cm, that is a percentage error of 4.6% in the y position of the beam center, and for photocell 3 the maximum power obtained was at $y=-0.77$ cm, thus giving us an error of 18.1%.

At $x=0$ cm, the maximum theoretical normalized optical power is 0.3811 for all photocells, where photocells 1 and 2 attain it at $y=0.65$ cm, and photocells 3 and 4 reach it at $y=-0.65$ cm. As can be seen from Fig. 22, photocells 1 and 2 gained maximum optical power at $y=0.83$ and 0.70 cm. The voltage percentage error for the preceding cases was 20.7% for photocell 1 and 26.2% for photocell 2. Photocells 3 and 4 gained maximum optical power at $y=-0.42$ and -0.74 cm, where their relative voltage percentage errors were evaluated to be 28.8% and 23.3%.

Figs. 18, 19 and 22 demonstrate discrepancies between the theoretical and experimental results in the values of the photo-voltage or optical power and the y position of the beam center. However, Figs. 20 and 21 have only shown a slight shift in the y position. To scan the beam spot along the y-axis of the quad-cell detector at a fixed x position, an initialization point has been selected such that the beam center is located at the upper right corner of photocell 1. This initial position of the beam center is adjusted manually until quarter of the power is acquired by photocell 1. However, with this setting, we have a position uncertainty of Δx and Δy leading to inaccuracies in both the x and y positions of the beam center. A shift in the x and y positions of the beam center can cause a deviation

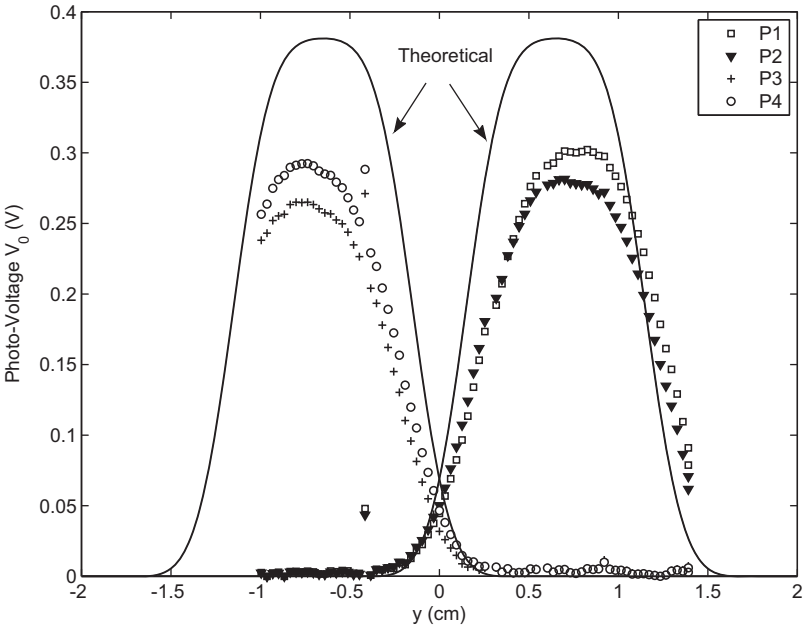

Fig. 22. Plot of photocell output voltage vs. y position of the center of the beam while setting the x position at 0 cm.

between the measured voltage and the corresponding theoretical normalized spatial optical power distribution.

In theory, the beam diameter is assumed to be exactly equal to the side of the square photodetector, and 99% of the optical power is contained within a beam spot of radius $1.5W(z)$, where $W(z)$ is the beam waist at the photodetector plane. These parameters are not necessarily guaranteed in the experiment. Practically, the beam radius was adjusted manually by gradually increasing it using the beam expander, until the beam spot fits into the active area of one photocell. The radius of the beam spot will be $0.5\,\text{cm}-\Delta\rho$ cm where less than 99% of the optical power is contained, thus causing a reduction in the optical power obtained in the experiment and that found theoretically.

In addition, the other source of error between the theoretical and practical results in terms of the shift in the y position and the difference in optical powers is due to having $\varepsilon = 0.1\,\text{cm} + \Delta\varepsilon$ cm and $\delta = 0.3\,\text{cm} + \Delta\delta$ cm. The errors $\Delta\varepsilon$ cm and $\Delta\delta$ cm are added distances due to the thickness of the ceramic wafer surrounding the Si detector, and the fact that the active area for FDS1010 is about $9.7\,\text{mm} \times 9.7\,\text{mm}$ which is less than the assumed theoretical active area of $1\,\text{cm} \times 1\,\text{cm}$. Since the quad-cell detector is placed on a metallic plate, there will be inevitable optical diffraction and reflections which cause a difference between the theoretical and measured power, especially along the scan at $x = 0$ cm where the beam center is passed entirely along the metallic gap. Moreover, imperfections in the horizontal alignment of the quad-cell detector plane and slight asymmetry around the center of the sensor at the receiver optics can be additional sources of error.

5. Conclusions

In this paper, a novel optical vibration sensing method using Gaussian beam analysis has been introduced. The closed form equations for the optical power covered by a certain area of overlap between the laser beam disk and one photodetector cell was also presented, as the disk moves throughout the entire x–y plane. Accordingly, the power distribution of a quad-cell photodetector array was evaluated, depending on the values for ε and δ. The simulation results of the power distribution for a quad-cell demonstrate the theoretical solution for the forward problem at hand. In addition, the results attained will enable us to approach the inverse problem as a next step to find a relationship between the optical power obtained experimentally and the current position of the laser beam. By sensing the position of the laser beam a vibration monitoring scheme can then be followed to estimate the vibration properties such as strength and direction.

References

[1] P. Rodriguez, S. Trivedi, F. Jin, J. Lorenzo, C. Wang, Z. Chen, J. Khurgin, B. Libbey, J. Habersat, High sensitivity pulsed laser vibrometer for surface vibration monitoring, Applied Physics Letters (2006), p. 1.
[2] C.W. de Silva, Vibration Fundamentals and Practice, CRC Press, New York, 2000.
[3] Z. Zhang, X. Bao, Continuous and damped vibration detection based on fiber diversity detection sensor by Rayleigh backscattering, Journal of Lightwave Technology 26 (7) (2008) 832.
[4] N.K. Verma, S. Kumar, Laser based optical sensor for vibration measurements, NDT&E International 39 (2006) 106–108.
[5] B.E.A. Saleh, Fundamentals of Photonics, Wiley, New York, 1991.
[6] Y. El-Ashi, R. Dhaouadi, T. Landolsi, Design of a novel optical vibrometer using Gaussian beam analysis, in: Proceeding of 5th International Symposium on Mechatronics and its Applications (ISMA08), 2008, pp. 3–4.
[7] A.E. Siegman, Lasers, University Science Books, Sausalito, California, 1986.
[8] 〈http://www.thorlabs.com〉, retrieved May 2009.